Potential TRIP/TWIP coupled effects in equiatomic CrCoNi medium-entropy alloy

L. Ding[1,2,3], A. Hilhorst[1], H. Idrissi[1,2], P.J. Jacques[1]

[1] UCLouvain, Institute of Mechanics, Materials and Civil Engineering, IMAP, Place Sainte Barbe 2, Louvain-la-Neuve, 1348, Belgium

[2] Electron Microscopy for Materials Science (EMAT) University of Antwerp 2020 Antwerp, Belgium

[3] Now at : Key laboratory for Light-weight Materials, Nanjing Tech University, Nanjing 211816, China

Abstract

High-entropy alloys (HEA) and medium-entropy alloys (MEA), containing multiple principal elements typically with equiatomic or near-equiatomic ratios, have drawn considerable attention due to their unique and promising mechanical profiles, such as high tensile strength, superior ductility and exceptional fracture toughness. However, the elementary mechanisms controlling the deformation and fracture of this new class of alloys still need complementary analyses. In the present study, the nucleation and growth mechanisms of deformation bands in the medium-entropy CrCoNi alloy were investigated by atomic-resolution scanning transmission electron microscopy (STEM). It was revealed that planar dislocation slip is the dominant deformation mode in the early stages of deformation. With increasing strain, both deformation twins and hexagonal close packed (HCP) lamella simultaneously appear. Careful analysis of the dislocations involved in these processes confirms that two different mechanisms are responsible for the nucleation of deformation bands in the CrCoNi alloy: the three-layer mechanism proposed by Mahajan et al. and the transformation from HCP phase to twin. Activation of multiple slip systems at larger deformation levels leads to the activation of deviation-based models, which contribute to the twin growth. It was also observed that many HCP bands remain and overlap with

nanoscale twins, leading to short range HCP-twin stackings, which contribute to the high work hardening rate of this alloy.

Keywords: Medium-entropy alloy; twinning; Martensitic transformation; Transmission electron microscopy (TEM); Plasticity

1. Introduction

High-entropy alloys (HEAs) and medium-entropy alloys (MEAs) have emerged as a new class of structural alloys due to their promising performance, including high strength, exceptional ductility and impressive fracture toughness [1-3]. Among various kinds of multi-component metallic alloys, the face centred cubic (FCC) ternary CrCoNi MEA alloy exhibits higher strength and ductility than those ones of the quaternary and quinary systems, with a tensile strength of almost 1 GPa, a fracture strain of ~ 0.6 and a fracture toughness above 200 MPa $m^{1/2}$ [3, 4]. Like other 3d-transition-metal-based HEAs and MEAs, it exhibits properties that are highly temperature-dependent, with the strength level increasing under cryogenic conditions [5, 6]. More surprisingly, both ductility and fracture toughness of CrCoNi alloy also increases with decreasing temperature [3]. The deformation behaviour of the CrCoNi alloy was studied by Laplanche et al. [7] and Miao et al. [8]. They showed that, at the early stage of deformation ($\varepsilon \leqslant 0.065$), planar slip of dislocations and dissociation of 1/2<110> perfect dislocations into 1/6<112> Schockley partial dislocations (SPDs) on {111} planes dominate the microstructure. At larger deformation levels, nano-twinning and few hexagonal close packed (HCP) lamella have been observed, the density of HCP laths increasing with the level of deformation, especially at cryogenic temperature [9, 10]. However, no clear relationship between both kinds of deformation bands was reported, even though they are responsible for the huge work-hardening rate of several kinds of alloys [11, 12].

Deformation twins in coarse-grained FCC metals are simplistically believed to form by the highly coordinated glide of identical SPDs on successive {111} close packed planes [13]. More fundamentally, it is necessary to assess how deformation twins nucleate from specific arrangements of partial dislocations. Various nucleation and growth mechanisms of deformation twins in FCC metals have been established, some of them being summarised hereunder.

(1) Venables pole mechanism

Venables [14] suggested that an a/2<100> perfect dislocation can dissociate under external stresses into a sessile a/3<111> Frank partial dislocation and an a/6<112> SPD on the conjugate slip plane, bounding an intrinsic stacking fault (SF). The equation of this dissociation is:

$$\frac{a}{2}[1\bar{1}0]_{(11\bar{1})} \rightarrow \frac{a}{3}[1\bar{1}1]_{sessile} + \frac{a}{6}[1\overline{12}]_{(1\bar{1}1)} \quad (1)$$

The a/3$[1\bar{1}1]$ Frank partial can serve as pole dislocation. The glissile SPD sweeps a helical path around the pole dislocation and changes its initial plane. If this process is repeated on every plane, a perfect twin structure without SFs is thus created.

(2) Models based on a deviation process

Cohen and Weertman [15] proposed that a perfect dislocation lying in the primary plane can dissociate into a sessile Frank partial dislocation and a glissile SPD when meeting a strong barrier such as a Lomer-Cottrell lock. The equation is as follow:

$$\frac{a}{2}[101]_{(1\overline{11})} \rightarrow \frac{a}{3}[1\bar{1}1]_{sessile} + \frac{a}{6}[1\overline{12}]_{(1\bar{1}1)} \quad (2)$$

On the other hand, Mori and Fujita [16] suggested a stair-rod cross-slip mechanism which consists in the dissociation of a SPD on the primary glide plane into a sessile stair-rod dislocation and another glissile SPD on the conjugate plane according to the following equation:

$$\frac{a}{6}[\bar{2}11]_{(111)} \rightarrow \frac{a}{6}[\overline{11}1]_{sessile} + \frac{a}{6}[\bar{1}21]_{(\overline{11}1)} \quad (3)$$

(3) The three-layer mechanism

Mahajan and Chin [17] proposed that two co-planar perfect dislocations could firstly split into four SPDs according to Equations (4a) and (4b):

$$\frac{a}{2}[\bar{1}01]_{(111)} \rightarrow \frac{a}{6}[\bar{2}11]_{(111)} + \frac{a}{6}[\overline{11}2]_{(111)} \quad (4a)$$

$$\frac{a}{2}[\bar{1}10]_{(111)} \rightarrow \frac{a}{6}[\bar{2}11]_{(111)} + \frac{a}{6}[\bar{1}2\bar{1}]_{(111)} \quad (4b)$$

Then, the interaction between these four SPDs can lead to the formation of an extrinsic stacking fault configuration that acts as a three-layer twin nucleus. The twin thickening is achieved by the overlap of these twin nuclei onto each other on the {111} planes. The dislocation reaction controlling the formation of three-layer twin nucleus can be expressed as follows:

$$\frac{a}{2}[10\bar{1}]_{(1\bar{1}1)} + \frac{a}{2}[011]_{(1\bar{1}1)} \rightarrow 3 \times \frac{a}{6}[1\overline{12}]_{(1\bar{1}1)} \quad (5)$$

Compared with mechanical twins, the simplistic view of HCP martensite formation consists in SPDs glide on every second {111} close packed plane. It has been reported that the pole mechanism, stair-rod cross-slip mechanism and three-layer mechanism could also be responsible for the formation of the HCP phase [18-20]. The main difference with the twinning mechanisms is the cross-slip of dislocations into the second adjacent plane.

In the literature, the small scale mechanisms controlling the formation of deformation twins have been the topic of intense work in traditional metallic alloys consisting of one to two prevalent matrix elements, such as twining-induced plasticity (TWIP) steels [21, 22] and nanocrystalline alloys [23]. Given the compositional complexity of high (medium) entropy alloys and the potentially resulting lattice distortion, short-range order, …, it can be anticipated that the twin nucleation and growth mechanisms are probably

different when compared to dilute solid solutions, constituting the majority of conventional alloys. However, these ones have been seldom addressed in the literature, even though the presence of deformation twins are critical for the improvement of the mechanical properties of these alloys [24]. Liu *et al.* [25] studied the twinning mechanism in an $FeCoNiCrAl_{0.1}$ high-entropy alloy by in-situ TEM. They demonstrated that mechanical twins are formed by SPDs generated by the cross-slip of full dislocations on the primary plane, gliding on successive {111} close packed planes following the reaction of Equation (2). However, the nature of the elementary extended defects involved in the very early stage of the twinning mechanism was not elucidated. Furthermore, experimental evidence regarding the mechanisms involved in the competition or the synergy between mechanically-induced twins or HCP transformation is lacking.

The present work aims at investigating the nucleation and growth mechanisms of deformation twins in an equatomic CrCoNi alloy through the identification of the dislocations involved at the onset of mechanical twinning. Conventional diffraction contrast imaging combined with aberration-corrected scanning transmission electron microscopy (STEM) were used to examine the atomic structure of the defects and to provide hints for the sequence of reactions between dislocations that possibly leads to the formation of mechanical twins and HCP phase.

2. Experimental procedure

A 1-kg ingot of equiatomic CrCoNi alloy was processed by vacuum induction melting from pure elements (>99.8% purity). The resulting composition was 33.9 at % Cr, 32.0 at % Co, 33.7 at % Ni, and traces of Fe, Mn, and Si (0.22, 0.09, and 0.06 %, respectively). The ingot was then hot-rolled at 1273 K down to a thickness of 5 mm and subsequently cold-rolled to a 1 mm thick sheet, resulting in more than 80% total deformation. After annealing at 1073 K for 1 hour, the microstructure was fully recrystallized with an average grain size of 3.5 µm. It is worth mentioning that such a recrystallization heat treatment is not prone to induce short range ordering as reported by Zhang et al.[26] for much longer heat treatments at a higher temperature. 70 mm x 10 mm tensile samples with a 30 mm gauge length and 6 mm gauge

width were machined by electrical discharge machining and deformed at a cross-head speed of 1 mm/min.

TEM specimens were prepared from initial or pre-deformed samples by electropolishing using a Struers TenuPol-5 machine opearated at 30 V. The electrolyte consisted of 95% acetic acid and 5% perchloric acid at a temperature of 12°C. Low and medium magnification TEM analyses of defects using diffraction contrast imaging were performed on a Tecnai F20 G^2 TEM operated at 200 kV while the atomic structure of the defects was investigated in a probe-corrected FEI Titan G2 60-300 "cubed" TEM operated at 300 kV.

3. Results

3.1 Tensile behaviour and general TEM observations

Fig. 1 shows the tensile true stress-true strain curve and the evolution of the work-hardening rate with strain of the CrCoNi alloy tested at room temperature. As already reported, this kind of alloy presents a large uniform strain and a high stress at the onset of necking resulting from its large work-hardening rate. Fig. 2 illustrates the initial microstructure of the investigated CrCoNi alloy.

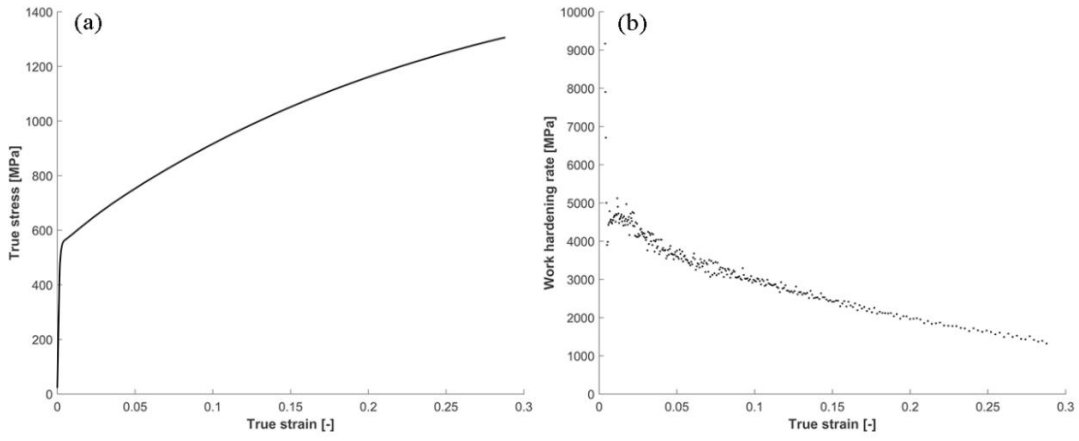

Figure 1 (a) True stress- true strain and (b) work hardening rate curves of the investigated CrCoNi alloy.

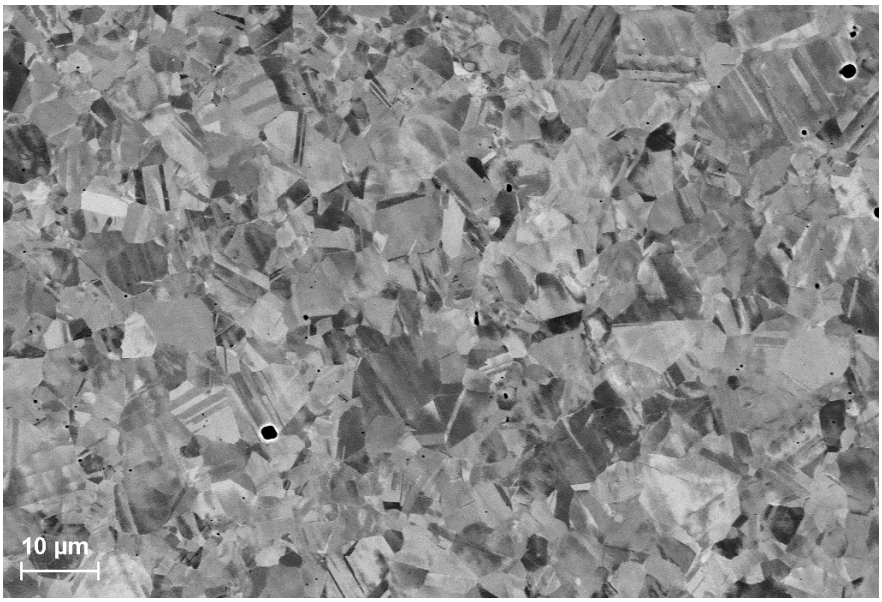

Figure 2 SEM micrograph of the initial microstructure of the investigated CrCoNi alloy.

The bright-field (BF) TEM micrographs of Fig. 3, obtained in two-beam diffraction conditions after different deformation levels illustrate the typical defects resulting from plastic deformation. The BF micrographs presented in Figs. 3(a-c) were acquired close to $[\bar{1}10]$ zone axis with a reflecting plane g=$1\bar{1}1$. The as-recrystallized sample (Fig. 3(a)) presents a very low density of dislocations and few dislocation pile-ups at the grain boundaries. After ε=0.02 (Fig. 3(b)), the dislocation density is significantly increased and planar slip of dislocations can be extensively observed as evidenced by the high fraction of dislocation pile-ups at grain boundaries. As the deformation increases to ε=0.1, a high density of extended stacking faults (SFs) can be observed in Fig. 3(c). Most of the SFs exhibit the same morphology with SF fringes parallel to the (111) plane, indicating that the deformation was controlled by dislocations activity in the (111) primary slip plane. On Fig. 3(d) corresponding to the edge-on view of the SFs acquired close to $[01\bar{1}]$ zone axis with a reflecting plane g=111, a high density of very thin lamella can be seen. The observed streaking of the diffraction spots along the <111> direction in the SAED pattern shown in the inset of Fig. 3(d) is often attributed to the presence of edge-on SFs and/or a high density of nano-twins [22, 27]. In the sample deformed to ε=0.2 (Fig. 3(e)), numerous thin deformation twins can be observed. In some grains (Fig. 3(f)), multiple twins lying in different planes could be observed. The corresponding $[\bar{1}10]$ selected area diffraction (SAED) patterns in the inset of Figs. 3(e and f) confirm the

presence of ∑3{111} coherent twin boundaries (CTBs) as evidenced by the typical superposition of two mirrored <110> diffraction patterns with respect to the {111} plane. Careful analysis of the deformation twins in Fig. 3(e) shows that the average twin thickness is about 5.4 ±3 nm.

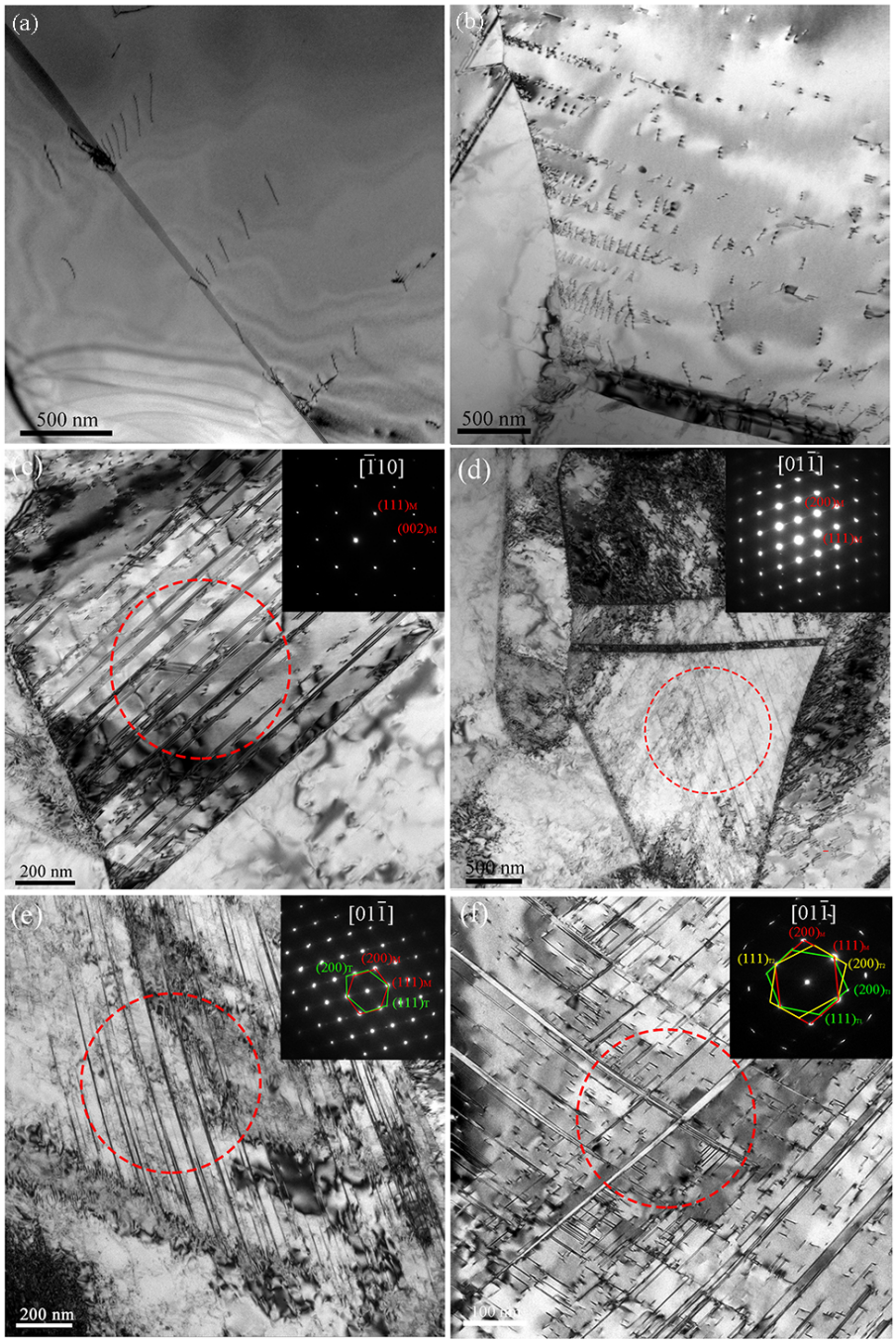

Figure 3 Bright-field TEM micrographs showing the microstructure evolution with true strain. (a) as recrystallized state, (b) ε=0.02*, (c-d)* ε=0.1 *and (e-f)* ε=0.2*. The SAED inserted in (c, d, e and f) correspond to the red dotted circles on the BF micrographs. The BF micrographs (a-c) were acquired close to the* $[\bar{1}10]$ *zone axis with a reflecting plane* g=$1\bar{1}1$*, while the BF micrographs (d-f) were acquired close to the* $[01\bar{1}]$ *zone axis with a reflecting plane* g=111*.*

3.2 Stacking fault energy

The stacking fault energy (SFE) was calculated by measuring the separation of partial dislocation pairs based on the following equation [28]:

$$d = \frac{G|b_p|^2}{8\pi\gamma} \cdot \frac{2-\nu}{1-\nu}\left(1 - \frac{2\nu\cos\theta}{2-\nu}\right) \qquad (6)$$

with G being the shear modulus, b_p the magnitude of the Burgers vector of partial dislocations and v the Poisson's ratio. A shear modulus of 87 GPa and Poisson's ratio of 0.3 were used for CrCoNi alloy [5]. Θ is the angle between the Burgers vector of the perfect dislocation and the dislocation line. The Burgers vector was measured as 0.179 nm. Fig. 4(a) shows a g-3g weak beam dark-field (WBDF) micrograph of dissociated dislocations in the sample deformed to ε=0.02, with g=$\bar{2}20$. An example of SPDs pair bounding a narrow intrinsic SF can be clearly observed. They are generated from the dissociation of a perfect dislocation in the (111) plane following the equation:

$$\frac{a}{2}[\bar{1}01]_{(111)} \rightarrow \frac{a}{6}[\bar{2}11]_{(111)} + \frac{a}{6}[\overline{11}2]_{(111)} \qquad (7)$$

Fig. 4(b) presents the experimentally measured partial dislocation separations (d) as a function of the angle Θ. According to Eq.(6), the SFE value is around 24 ± 3 mJ m^{-2}, which corresponds to previous experimental estimation (22 ± 4 mJ m^{-2})[7].

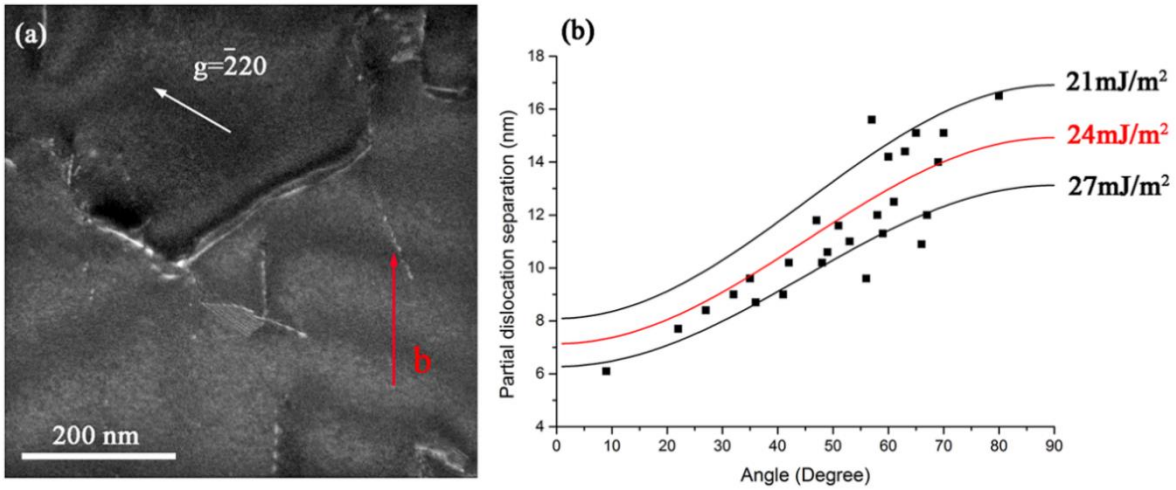

Figure 4 (a) TEM-WBDF micrograph of the dissociated dislocations taken in the sample deformed to ε=0.02, the red arrow indicates the Burgers vector of the full dislocation. (b) Separation distance between the two SPDs as a

function of the angle between the dislocation line and the Burgers vector of the full dislocation. The three curves represent partial dislocation separations calculated using Eq.(6) for different SFEs.

3.3 Twin and hcp nucleation mechanisms

The nucleation mechanisms were investigated in the sample deformed to ε=0.1, which presents a high density of SFs. Atomic resolution HAADF-STEM was used to reveal specific dislocation reactions. Fig. 5(a) exhibits low magnification HAADF-STEM micrograph of a planar defect present in the same zone as the one of Fig. 3(d), while the atomic scale resolution HAADF-STEM micrographs of Figs. 5(b, d and f) correspond to three different regions of this defect. These micrographs confirm that this defect corresponds to an extrinsic-intrinsic fault pair. Furthermore, since this fault pair stops within the grain, it was possible to characterize the dislocations bounding the SFs. For the two partial dislocations bounding the extrinsic SF (ESF), two Burgers circuits were drawn according to the guidelines proposed by Howe [29], as shown on Fig. 5(c). Both closure failure vectors $\overline{\mathrm{FSe}}$ and $\overline{\mathrm{FSs}}$ are measured as one lattice spacing, indicating that the circuit encloses one 90° partial dislocation and one 30° partial dislocation lying in immediately adjacent glide planes. In order to identify the partial dislocation associated to the transformation from ESF to intrinsic SF (ISF), another Burgers circuit [30] is drawn and shows that b=a/6[$\bar{2}11$] (30° partial) (see more details in the supplementary material). The partial dislocation delimiting the ISF in Fig. 5(g) is identified as b=a/6[$\bar{2}11$] (30° partial) based on the Burgers circuit. It is worth noting that the dislocations observed here are in perfect agreement with the extrinsic-intrinsic fault pair involved in the three-layer mechanism proposed by Mahajan and Chin [17]. Indeed, the extrinsic-intrinsic fault pair is an intermediate step preceding the formation of the three-layer twin embryo as shown on the schematic of Fig. 5(h).

Fig. 6(a) shows a low-magnification HAADF-STEM micrograph of another planar defect at ε=0.1. Here, atomic resolution HAADF-STEM micrographs in four different regions (Figs. 6(b, d, f and h)) confirm that this defect corresponds to a three-layer twin embryo. Indeed, at the edge of the lamellae (Fig. 6(b)), a nanotwin with a thickness of three atomic layers can be observed. In Fig. 6(d), the three-layer twin transforms into an ESF, which transforms itself into an ISF (Fig. 6(f)) that stops in the matrix (Fig. 6(h)).

Again, the method of Howe et al. [29] was used to identify the partials at the tip of the three-layer twin as shown in Fig. 6(c). In this figure, the closure failure vectors $\overline{\mathrm{FSe}}$ and $\overline{\mathrm{FSs}}$ are measured as one lattice spacing and two lattice spacings, respectively, indicating the presence of one 90° and two 30° SPDs. Note that the net Burgers vector of the three partials at the tip of the three-layer twin is zero (b1+b2+b3=0) as evidenced by the Burgers circuit with no closure failure, (as shown by the white dash line in Fig.6(c)). Furthermore, the three partial dislocations associated to the transformations 3-layer twin→ESF, ESF→ISF and ISF→matrix are identified as a/6[$\bar{2}11$] (30°) SPDs (see the Burgers circuits in Figs. 6(c, e and g) and supplementary materials for more details).

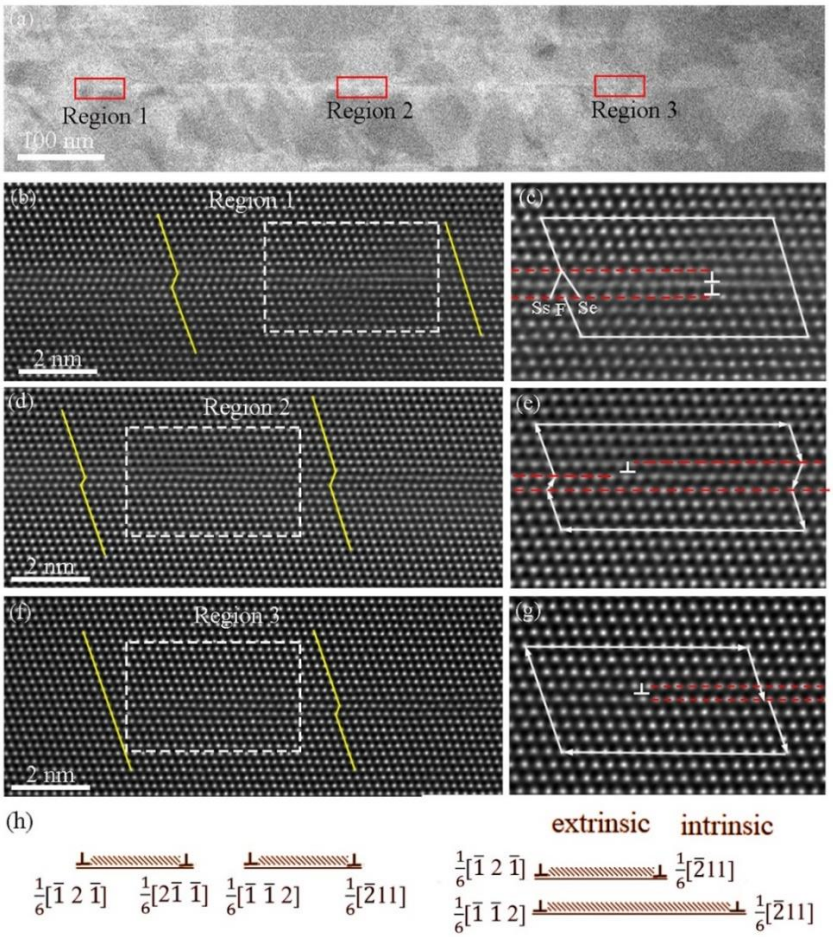

Figure 5 (a) Low-magnification HAADF-STEM micrograph of a SF formed in the sample deformed to ε=0.1. (b, d and f) show the atomic-resolution HAADF-STEM micrographs in three different regions of the SF, marked by red rectangles in (a). The stacking sequence of the atomic planes is marked by the yellow lines in (b, d and f). (c, e and g) show the enlarged HAADF-STEM of the region marked by the white dotted rectangles in (b, d and f). the SFs regions are marked by the red dotted lines in (c, e and g), (h) Schematic illustration of the formation of extrinsic-intrinsic fault pair.

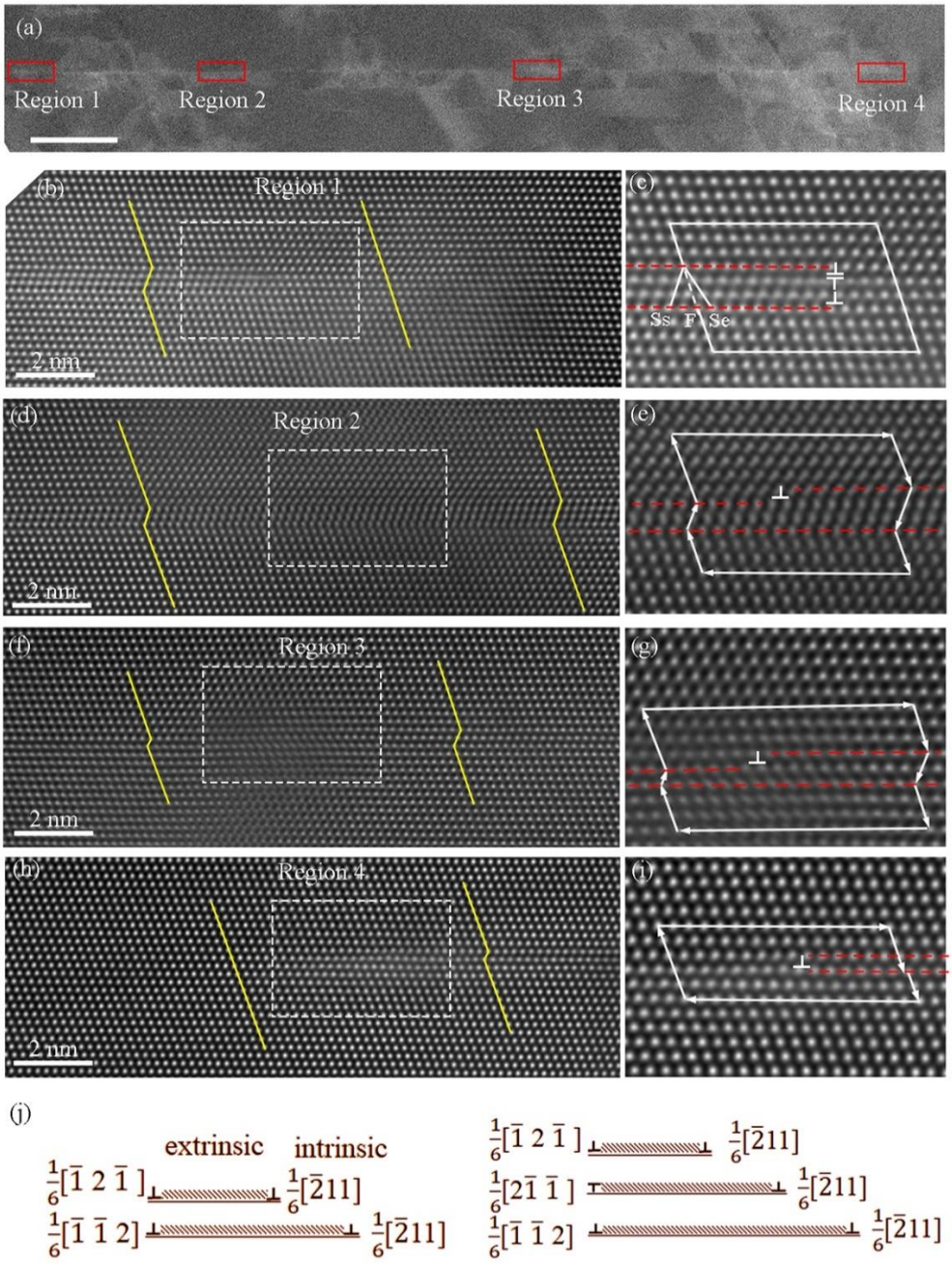

Figure 6 (a) Low magnification HAADF-STEM micrograph of a SF/nano-twin lamella formed in the sample deformed to ε=0.1. (b, d, f and h) show the atomic-resolution HAADF-STEM micrographs in four different regions of the SF, the four regions are marked by red rectangles in (a). The stacking sequence of the atomic planes is highlighted by the yellow lines in (b, d, f and h). (c, e, g and i) show the enlarged HAADF-STEM of the region marked by the white dotted rectangles in (b, d and f and h). the SF/nano-twin regions are marked by the red dotted lines in (c, e, g and i). (j) Schematic illustration of the fault configurations of the three-layer twin.

The observations provided in Figs. 5 and 6 thus confirm that the mechanism proposed by Mahajan and Chin [17] is responsible for the formation of the ESFs and three-layer twin embryo in the present work. Indeed, the interaction of the two co-planar glide dislocations ($a/2[\bar{1}01]_{(111)}$ and $a/2[\bar{1}10]_{(111)}$) leads to the formation of an extrinsic-intrinsic fault pair (Fig. 5) which transforms into a three-layer twin following Eq.(5), see also the schematic in Fig. 5(h). More than 10 extrinsic-intrinsic fault pairs and three-layer twin embryos supporting the Mahajan and Chin mechanism were found and characterized. To the best of the author's knowledge, this is the first time that the three-layers mechanism of Mahajan and Chin [17] is confirmed at the atomic scale in high-entropy alloys.

Beside the formation of mechanical twins, some HCP martensite lamella have also been detected as shown in Fig. 7. In this figure, 4-layer HCP lamellae involving two SFs separated by one atomic layer can be observed (Fig. 7(b)). The 4-layer HCP transforms into a single ISF (Fig. 7(b)) which stops within the grain (Fig. 7(f)). In Fig. 7(c), the two partials at the tip of the four-layer HCP phase are identified as a/6[$\bar{1}2\bar{1}$] (30°) and a/6[$\bar{1}\bar{1}2$] (90°) while the two dislocations delimiting the two non-neighbouring SFs in Fig. 7(d) and Fig. 7(f) are 30° partials with b=a/6[$\bar{2}11$], respectively, see Figs. 7(e and g). This four-layer HCP configuration corresponds well to the early stage of the HCP nucleation mechanism proposed by Mahajan et al. [20], see also the schematic of Fig. 7(h).

HAADF-STEM micrographs of Fig. 8 show the formation of 6-layer and 8-layer HCP laths. The 6-layer HCP lath is formed by overlapping of a 4-layer HCP lath with a SF at non-neighbouring plane (Figs. 8(a) and 8(e)) while the 8-layer HCP lath is formed by overlapping of a 4-layer HCP lamella with two SFs in non-neighbouring planes in both sides of the 4-layer HCP lath (Figs. 8(c) and 8(f)). The two dislocations bounding the four-layer HCP lath are identified as 90° partial and a 30° partial dislocations with Burgers vectors a/6[$\bar{1}2\bar{1}$] (30°) and a/6[$\bar{1}\bar{1}2$] (90°), respectively (Figs. 8(b and d)). These partials are similar to those identified at the tip of the four-layer HCP lath of Fig. 7. It can thus be concluded that the transformation from four-layer to six-layer HCP following the model proposed by Mahajan et al. [20] did not occur here because the third 30° partial with b=a/6[$2\bar{1}\bar{1}$] which should form a compact dislocation core with the other two partials in Figs. 8(b) and 8(d) is not observed here. The 6-layer and 8-layer HCP

laths in Fig. 8 were formed by the preferential nucleation and glide of ISFs at the vicinity of pre-existing four-layer HCP lamella. The origin of such feature will be discussed later. It is worth noting that HCP laths thicker than eight layers were not observed in the present study. Furthermore, further characterization of numerous defects has shown that the fraction of HCP laths is rather small (accounting for 10% of the total number of planar defects including twins and HCP phase).

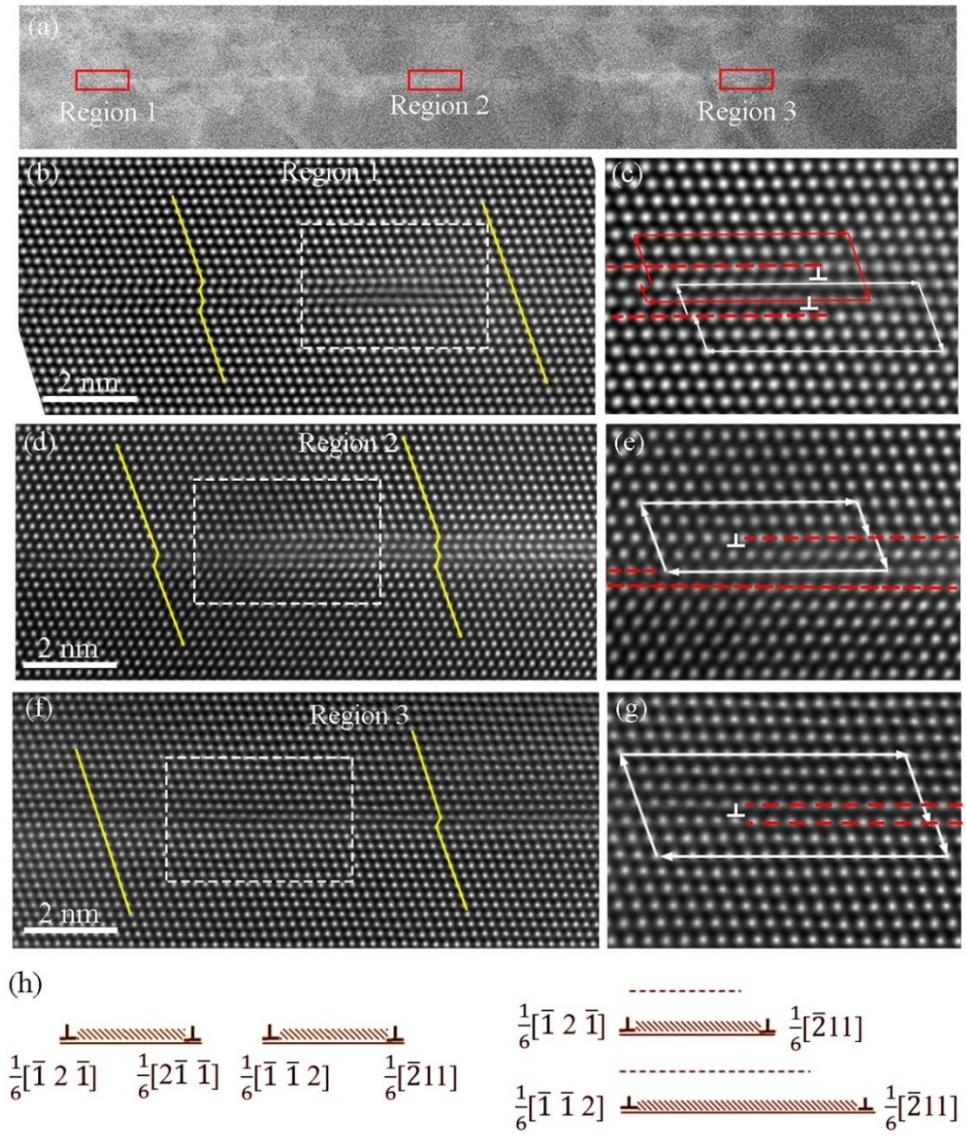

Figure 7 (a) Low magnification HAADF-STEM micrograph of a four-layer HCP lamella formed in the sample deformed to ε=0.1. (b, d and f) show the atomic-resolution HAADF-STEM micrographs in three different regions of the four-layer HCP, the three regions are marked by red rectangles in (a). The stacking sequence of the atomic planes is highlighted by the yellow lines in (b, d and f). (c, e and g) show the enlarged HAADF-STEM of the regions marked by the white dotted rectangles in (b, d and f). The SFs regions are marked by the red dotted lines in (c, e and g). (h) Schematic illustration of the fault configurations of the four-layer HCP.

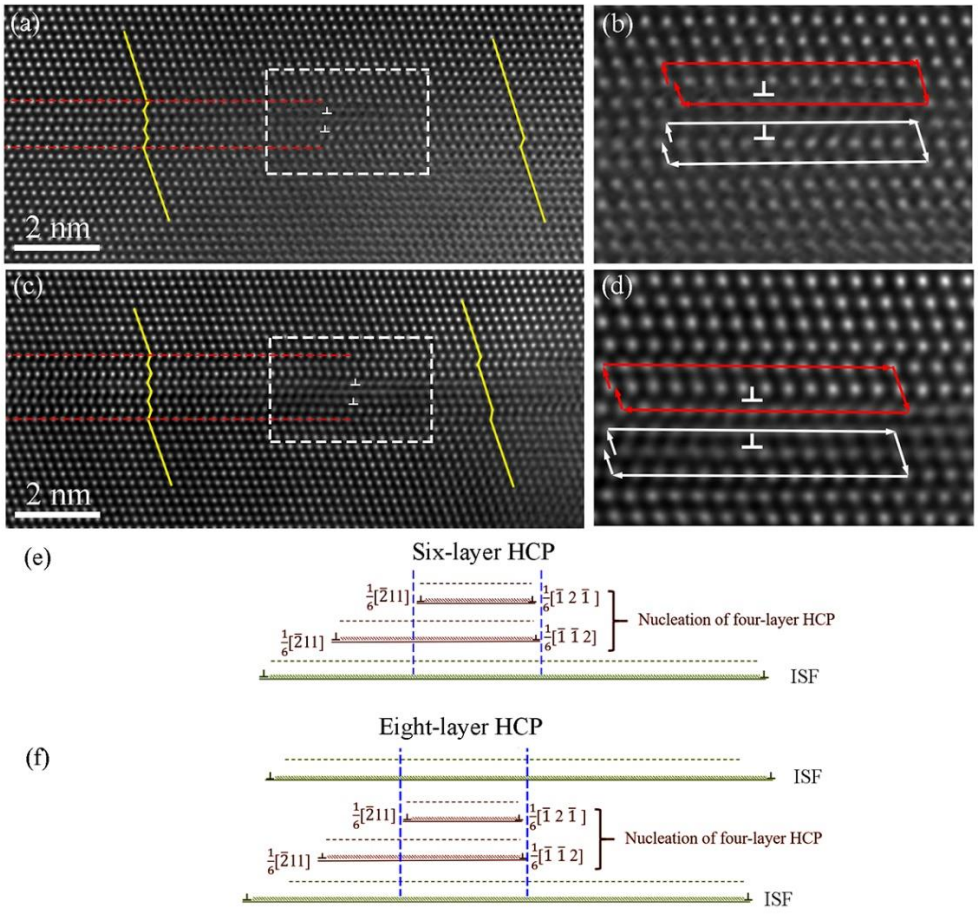

Figure 8 Atomic resolution HAADF-STEM micrographs showing the formation of six-layer (a) and eight-layer (c) HCP phase. (b and d) show the enlarged HAADF-STEM of the regions marked by the white dotted rectangles in (a and c). (e) Schematic illustration of the formation of six-layer and eight-layer HCP.

Finally, careful analysis of some HCP laths at the atomic scale reveals the HCP⟶twin transformation, as shown in Fig. 9. In this figure, the sequence of planar defects (Fig. 9(a)) involving 6-layer-HCP → 6-layer twin → 7-layer twin → 4-layer HCP can be observed (Figs. 9(b-c)). Figs. 9(d-e) show that the transformation from 6-layer HCP to 6-layer twin is due to the nucleation and glide of three SPDs (marked by the red lines in Fig. 9(d)) in the planes separating the SFs of the HCP phase. In Fig. 9(e), the same phenomena occurred in the opposite direction but with the formation of one new SF in the 6-layer upper twin boundary leading to seven-layer twin. The transformation of this 7-layer twin into the 4-layer HCP in this figure is due to the fact that one SF of the 6-layer HCP lamella (marked by white line in the bottom

of the twin lamella in Fig. 9(e)) stops close to other SPDs. The observations of Fig. 9 indicate that the HCP →twin transformation can occur in the present alloy via twin formation within the HCP laths. This process involves the nucleation and glide of SPDs between the SFs of the HCP phase, leading to the formation of HCP and twin laminated substructures as it can be seen in Fig. 10. Some ISFs can also be observed in this figure. The HCP laths exhibit a coherent orientation relationship (OR) which can be identified as $(0001)_{HCP}$ // $(111)_{twin}$ and $[11\text{-}20]_{HCP}$ // $[1\text{-}10]_{twin}$, in agreement with previous experimental observations [8]. Therefore, the overlapping between HCP phase and twins can also contribute to the growth of deformation twins.

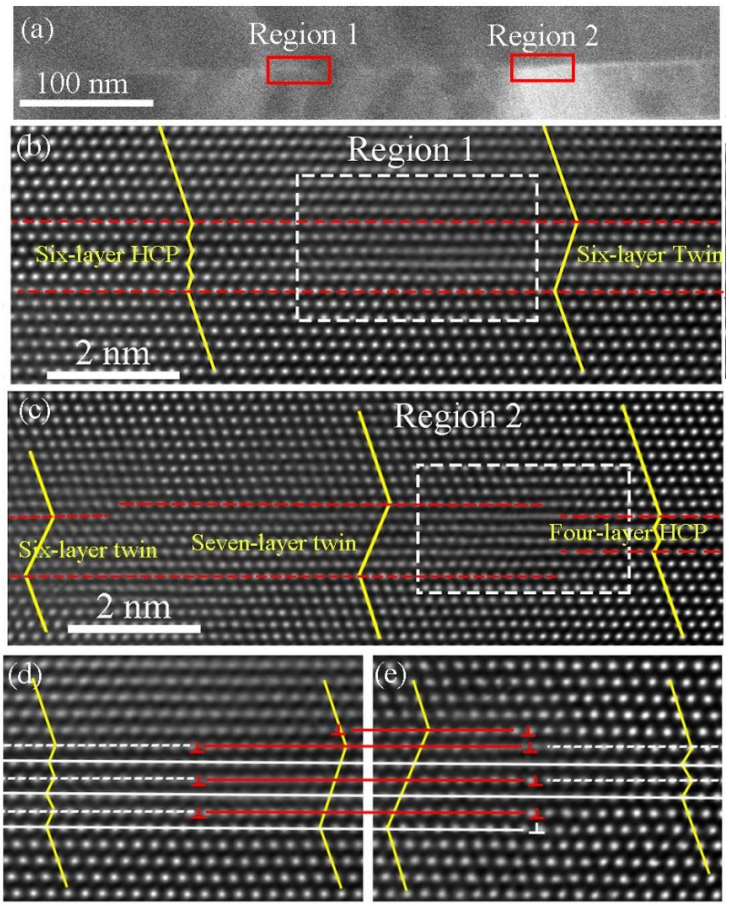

Figure 9 (a) Low magnification HAADF-STEM micrograph of an HCP/nano-twin lamella formed in the sample deformed to ε=0.1. (b and c) present the atomic-resolution HAADF-STEM micrographs highlighting the transformation of the six-layer HCP phase to six-layer twin and the transformation from the six-layer twin to four-layer HCP phase. The two regions in (b and c) are marked by red rectangles in (a). (c and e) are the enlarged HAADF-STEM micrographs obtained in the white dotted rectangles in (b and c). The shifted and non-shifted atomic planes are marked by the white and dotted white lines.

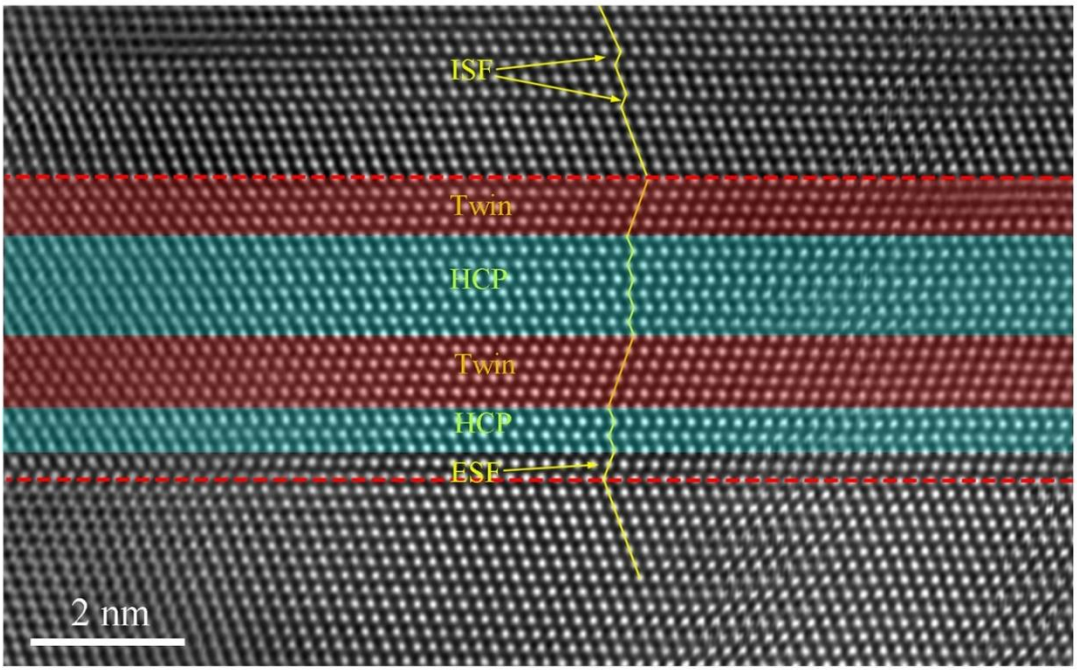

Figure 10 HAADF-STEM micrograph showing the overlapping of twins and HCP phase in the sample deformed to ε=0.1.

3.4 The growth mechanism of deformation twins

The BF micrograph of Fig. 11(a) corresponds to the sample deformed to ε=0.2 in which dislocations, twins and SFs were observed on Fig. 3 (f). In Fig. 11(a), stair-rod dislocations (highlighted by dark arrows) are formed at the intersection between a twin embryo in the (111) plane and SFs located in the $(\overline{1}\overline{1}1)$ plane.

The high resolution HAADF-STEM micrograph of Fig. 11(b) shows the interaction of one ISF in the $(\overline{1}\overline{1}1)$ plane with twin boundary leading to the formation of a stair-rod dislocation at the CTB plane. This is in agreement with the stair-rod cross-slip mechanism proposed by Mori and Fujita [16] following the reaction of Eq. (3). In the right side of Fig. 11(b), a Frank dislocation with Burgers vector of type a/3[111] is identified using Burgers circuit in the DSC lattice [31]. This is also confirmed in the inverse FFT inset where the extra half-plane of this dislocation is parallel to the twinning plane. The origin of the Frank dislocation at the TB can be attributed to the model based on a deviation process proposed by Cohen and Weertman [15] following the reaction of Eq. (2).

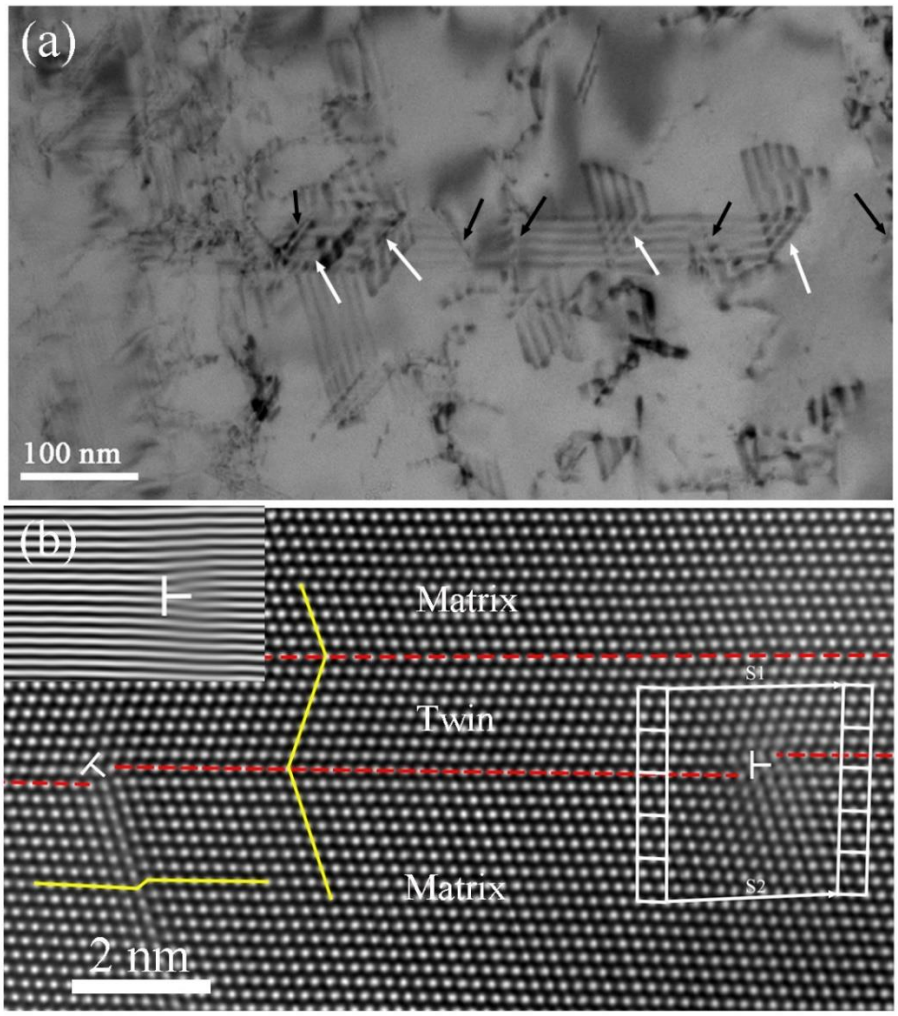

Figure 11 For sample deformed to ε=0.2, (a) two beam BF micrograph after tilting the region of Fig. 3(f) away from the <110> zone axis; (b) HAADF-STEM micrograph showing the interaction of the SF and the primary twin.

4 Discussion

The investigated CrCoNi alloy exhibits a large work hardening capacity due to the activation of different deformation mechanisms during straining. In the early stage of deformation, planar dislocation slip is the dominant deformation mode. Indeed, gliding dislocations are strongly localized on a distinct set of {111} planes, involving the formation of dislocation pile-ups at the grain boundaries. Furthermore, high density of extended SFs is formed due to the dissociation of dislocations. The increase of plastic strain then leads to the formation of mechanical twins and HCP laths. The former largely dominates at a strain level of 0.1 (i.e. twins account for about 90% of the total number of deformation bands). However, local

analysis shows that these so-called twins actually exhibit a regular stacking of nano-sized twins and HCP laths. Such feature most probably participates to the large work hardening rate of CrCoNi alloy by the combination at the nanoscale of twinning-induced plasticity (TWIP) and transformation-induced plasticity (TRIP) effects. Indeed, considering only the influence of the density of interfaces created by the formation of deformation bands (twins in the present case) for what is called 'dynamic Hall-Petch effect' is not enough to account for the influence of these bands on the work hardening rate. The internal structure of the deformation bands drastically influences the work hardening as shown in the case of TWIP steels for which an explicit relationship between the twin internal structure and the resulting work hardening rate was established[32]. It can be anticipated that the nano-laminated composite structure of twin and HCP layers also acts as strengthening inclusions in the case of CrCoNi alloy. Furthermore, the HCP lamella have been reported to be very effective barriers for dislocation motion since transmission of edge-component dislocations into the HCP phase would require the activation of dislocations with a component along [0001], requiring either <c> or <c+a> dislocations. These types of dislocations typically have a very large critical resolved shear stress in the HCP structure [33]. Therefore, the TRIP effect including HCP laths has generally a higher strengthening potential than mechanical twinning [34]. Finally, the HCP layers could act as source of twinning, also improving the strength – ductility balance. Understanding the elementary mechanisms controlling the nucleation of mechanically induced twins and HCP laths is thus of key importance in order to improve the strength-ductility trade-off of HEAs and MEAs. Very thin HCP laths have rarely been reported in other alloys, such as stainless TRIP steels [34] and TRIP-assisted high-entropy alloys [35]. Short-range HCP-stacking twin boundaries was also reported by Yu et al. using atomistic simulations and by TEM analysis in HEAs similar to the present work [36]. However, experimental evidences of the elementary mechanisms controlling this phenomenon were still missing before the present work bringing experimental evidences.

In this work, different mechanisms have been observed owing to detailed characterization of the extended defects at the atomic scale. At the early stage of deformation, the interactions between co-planar dislocations lead to the formation of a large amount of extrinsic-intrinsic fault pairs and three-

layer twin nuclei, in agreement with the twinning mechanism proposed by Mahajan and Chin [17]. Mahajan and Green [20] also proposed that their mechanism could explain the formation of four- and six-layer HCP lamellae. However, only four-layer HCP lamellae involving dislocations formed by this mechanism have been observed in the present work. The 6-layer HCP and 8-layer HCP observed in Figs. 8(a and c) were formed by the overlapping of the 4-layer HCP with ISFs nucleated from other sources. The 8-layer HCP is the largest thickness observed for HCP lamella in this work. Therefore, the reaction at the origin of the three SPDs ($a/2<1\bar{1}0> + a/2<10\bar{1}> \rightarrow 3 \times a/6<2\overline{11}>$) involved in the six-layer HCP embryo is not occurring in the present alloy. These observations indicate that the energies of ESF and the 4-layer HCP lamella are not much different, leading to a synergy between these two defects. Local changes of the environment at the reaction site between the co-planar dislocations could then lead to the formation of the second SPD in the n+1 plane (i.e. ESF) or n+2 plane (i.e. 4-layer HCP). To the best of the author's knowledge, this is the first time that the Mahajan et al. [17, 20] three-layer mechanism for TWIP and TRIP effects is observed at the atomic scale in the case of MEAs.

It is worth noting that the simultaneous observation of twins and HCP as deformation mechanisms is not common in FCC metallic alloys. In the present case of the CrCoNi alloy, one hypothesis could be local changes of SFE due to some chemical ordering. Thus, the reacting dislocations in the Mahajan et al. [17, 20] mechanism would cross-slip to the first or the second adjacent plane depending on local changes of the separation distance between the partials. It has been demonstrated in the literature that with decreasing SFE, the active plasticity mode changes from dislocation glide to mechanical twinning and then to martensitic transformation (HCP) [37]. Lee *et al.* [38] and Remy *et al.* [39] proposed an empirical but ambiguous criterion of SFE of 20 mJ m^{-2} for HCP transformation vs twinning. The SFE of the investigated CrCoNi alloy is around 24 ± 4 mJ m^{-2}, not too far from the proposed transition between both deformation mechanisms. Furthermore, SFE could exhibit large scattering even when measured in the same alloy. For example, SFE measured in the case of stainless steel 304 ranges from 8 to 40 mJ m^{-2} [40] and from 14.2 to 78 mJ m^{-2} for stainless steel 316 [41]. Smith et al. [42] also reported that CrCoFeMnNi high-entropy alloy has a significant variation of its SFE (stacking fault width ranging from 1 nm to 9 nm),

assumed as resulting from the complex solute configurations of high-entropy alloys. Finally, it is worth reminding that two kinds of stackings faults intervene in the mechanisms of formation of twins and HCP martensite, i.e. intrinsic and extrinsic stacking faults. Complementary analysis would therefore requires estimating not only the intrinsic stacking fault energy, but also the extrinsic one. Furthermore, it has already been reported that the temperature evolution of the energies of these two defects are not identical [43, 44], which could potentially dictate the evolution of the work hardening rate with temperature of the present alloy.

Further considering the presence of very thin HCP lamella, it was observed that once they are formed, they can transform into nanotwins via the nucleation of new SPDs within the HCP phase (Figure 9). The transformation of 4-layer HCP phase (two SPDs on non-neighbouring glide) into twin was firstly predicted using molecular dynamics (MD) simulations by Wang et al. [45] where transformation occurs through the nucleation of a dislocation loop in the faulted region under high stress. Xu et al. [46] and Wang et al. [47] reported experimental evidence of the formation of twin nuclei in HCP laths by the emission of a SPD between two SFs in coarse-grained Ni-Co-based superalloy and nanocrystalline Pt, respectively. Yu et al.[36] used DFT calculation and kinetic Monte Carlo (KMC) simulation to show that twins could form within the HCP laths in the $FeCrNiCoAl_{0.36}$ high entropy alloy due to the competing FCC/HCP phase stability. The observations shown in Fig. 11 thus constitutes a first of kind experimental evidence of such phenomena in MEAs. However, the nature of the nucleation sites of such SPDs remains obscure. Several assumptions can be made such as pre-existing defects within the HCP phase due for example to local fluctuations of chemical order leading to local changes of SFE and local increase of stress concentrations, defects at the FCC/HCP interface or defects arising from the transmission of incoming dislocation through this interface. Further advanced TEM characterization would be needed to elucidate this behaviour. On the other hand, in the absence of these sources, HCP lamella could remain and overlap with nanotwins, forming short range twin-HCP stacking (Figure 10). Figure 12 proposes a summarizing illustration of the mechanisms leading to the formation of twins and twin-HCP stacking observed in the present work.

The overlapping of twins with HCP lamella and SFs leads to the growth of thicker but defective twins or HCP bands with a high capacity to reduce the mean free path of dislocations while inducing hard inclusions strengthening [32]. In some grains, when multiple slips are activated, pole mechanisms based on deviation process contribute to the growth of deformation twins. Both the stair-rod cross-slip mechanism [16] and the models based on deviation process proposed by Cohen and Weertman [15] are observed. Indeed, for the first mechanism, widely dissociated incoming dislocations (i.e. small SFE) glide towards the twin nuclei, where only the leading partial will dissociate into a stair-rod sessile dislocation (Fig. 11) and a glissile SPD in the twin boundary following Eq. (3). For the second mechanism, the dissociation distance is smaller (i.e. high SFE). The SPDs of the extended coming dislocation can thus recombine into a perfect dislocation and re-dissociate into a Frank sessile dislocation (Fig. 11) and a glissile SPD in the TB plane following Eq.(2).

It is worth noting that the average twin thickness of the CrCoNi alloy used in the present work (~5 nm at ε=0.1) is much smaller when compared with TWIP steels such as Fe-Mn-Si-Al TWIP steel (100-700 nm at ε=0.1) [22] and Fe-Mn-C TWIP steel (40-100 nm at ε=0.1) [21]. This can be explained by the 'easy' nucleation of SFs and the co-existence of nanoscale twins and HCP lamella. Previous in-situ straining experiments performed in the case of CrCoNi alloy have shown that the activation of SFs is much easier than planar slip of ½<110> dislocation [4]. This might facilitate the formation of high density of twin nuclei, which refine the distribution of twins. The sluggish movement of extended dislocations can delay the growth of deformation twins, resulting in rather thin mechanical twins. Therefore, a high density of nano-sized twins and twin-HCP lamellae are formed. The very small thickness of the planar defects could increase the back stress. Indeed, very high resolved shear stresses are required to activate dislocations in such small lamella, increasing the back stress and the strain hardening capacity.

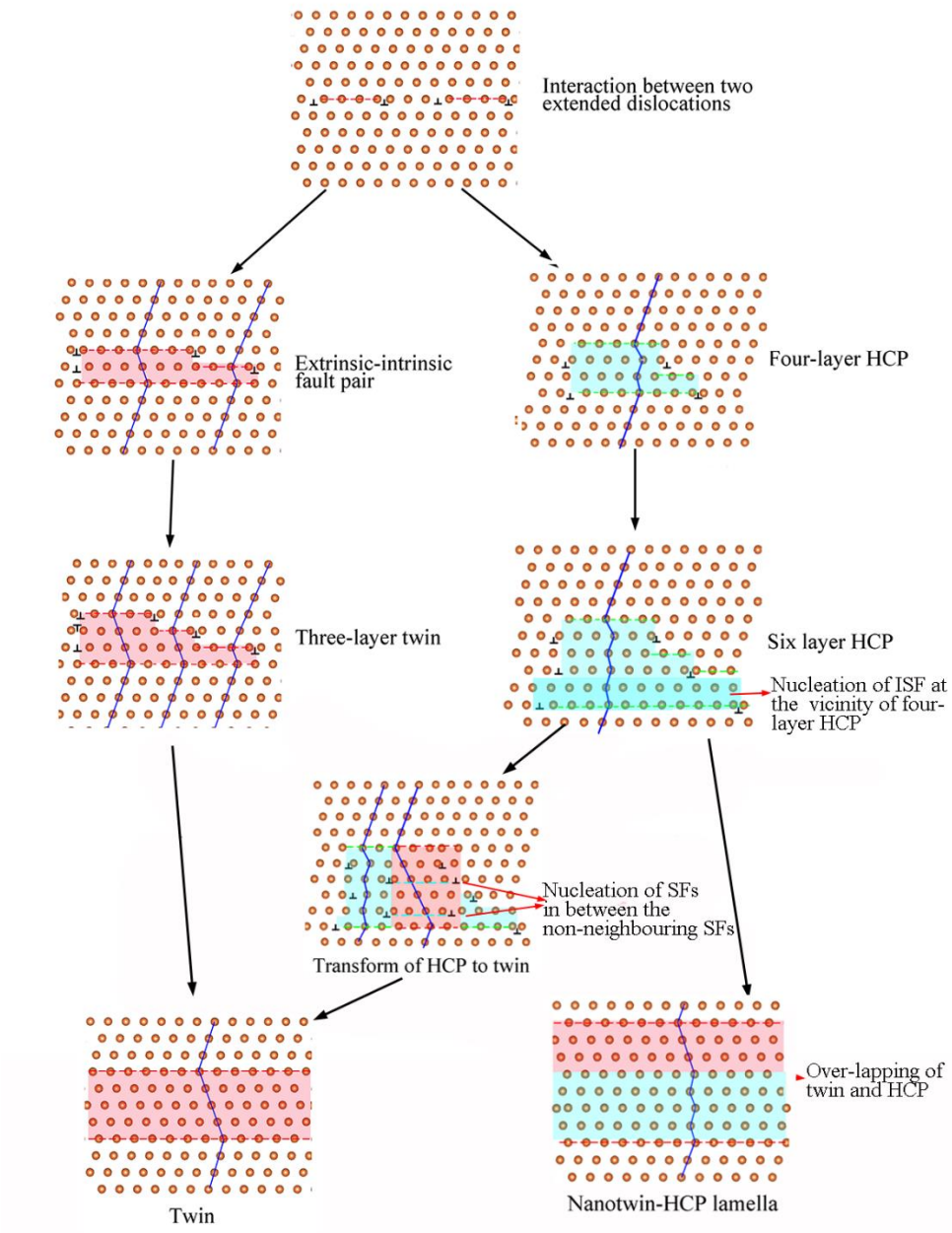

Figure 12 Schematic illustration of the nucleation mechanism of the twin and HCP phase

Conclusion

The present work focuses on the experimental investigation of the small-scale elementary mechanisms controlling TWIP and TRIP effects in equiatomic CrCoNi medium-entropy alloy. The results can be summarized as follows:

1. The alloy exhibits a large work hardening capacity due to the activation of different deformation modes during straining. In the early stage of deformation, planar dislocation slip dominates the plasticity. With the increase of plastic strain, nanoscale twins and HCP lamellae are formed. Such behaviour could significantly promote the work hardening capacity through the combination of TWIP and TRIP effects.
2. Two mechanisms are responsible for the nucleation of deformation twins in the CrCoNi alloy: i) the three-layer mechanism of Mahajan [17] involving the interaction between coplanar dislocations is the main mechanism controlling twin nucleation; ii) the transformation of HCP phase to twin, which is caused by the nucleation of SFs in between the non-neighbouring SFs within the HCP lath. The nucleation of HCP phase in the matrix is also controlled by the three-layer mechanism of Mahajan [20].
3. At higher deformation level, multiple slip leads to the activation of twinning mechanisms based on deviation models which contribute to the twin growth.
4. The deformation twins in the CrCoNi alloy are rather thin compared to common TWIP steels. The easy activation of SFs, the presence of short-range twin-HCP stacking and the sluggish movement of extended dislocations could explain the formation of high density of thin deformation twins.

Acknowledgments

The research was funded by the Walloon Region under the agreement No. 1610154-EntroTough in the context of the 2016 WallInnov call. H. Idrissi is mandated by the Belgian National Fund for Scientific Research (FRS-FNRS).

References

[1] J.-W. Yeh, S.-K. Chen, S.-J. Lin, J.-Y. Gan, T.-S. Chin, T.-T. Shun, C.-H. Tsau, S.-Y. Chang, Nanostructured High-Entropy Alloys with Multiple Principal Elements: Novel Alloy Design Concepts and Outcomes, Adv. Eng. Mater. 6 (2004) 299-303.

[2] B. Gludovatz, A. Hohenwarter, D. Catoor, E.H. Chang, Easo P. George, R.O. Ritchie, A fracture-resistant high-entropy alloy for cryogenic applications, Science 345 (2014) 1153-1158.

[3] B. Gludovatz, A. Hohenwarter, K.V. Thurston, H. Bei, Z. Wu, E.P. George, R.O. Ritchie, Exceptional damage-tolerance of a medium-entropy alloy CrCoNi at cryogenic temperatures, Nat. Commun. 7 (2016) 10602.

[4] Z. Zhang, H. Sheng, Z. Wang, B. Gludovatz, Z. Zhang, E.P. George, Q. Yu, S.X. Mao, R.O. Ritchie, Dislocation mechanisms and 3D twin architectures generate exceptional strength-ductility-toughness combination in CrCoNi medium-entropy alloy, Nat. Commun. 8 (2017) 14390.

[5] Z. Wu, H. Bei, G.M. Pharr, E.P. George, Temperature dependence of the mechanical properties of equiatomic solid solution alloys with face-centered cubic crystal structures, Acta Mater. 81 (2014) 428-441.

[6] Z.F. He, N. Jia, D. Ma, H.L. Yan, Z.M. Li, D. Raabe, Joint contribution of transformation and twinning to the high strength-ductility combination of a FeMnCoCr high entropy alloy at cryogenic temperatures, Mater. Sci. Eng. A. 759 (2019) 437-447.

[7] G. Laplanche, A. Kostka, C. Reinhart, J. Hunfeld, G. Eggeler, E.P. George, Reasons for the superior mechanical properties of medium-entropy CrCoNi compared to high-entropy CrMnFeCoNi, Acta Mater. 128 (2017) 292-303.

[8] J. Miao, C.E. Slone, T.M. Smith, C. Niu, H. Bei, M. Ghazisaeidi, G.M. Pharr, M.J. Mills, The evolution of the deformation substructure in a Ni-Co-Cr equiatomic solid solution alloy, Acta Mater. 132 (2017) 35-48.

[9] C.E. Slone, S. Chakraborty, J. Miao, E.P. George, M.J. Mills, S.R. Niezgoda, Influence of deformation induced nanoscale twinning and FCC-HCP transformation on hardening and texture development in medium-entropy CrCoNi alloy, Acta Mater. 158 (2018) 38-52.

[10] H.W. Deng, Z.M. Xie, B.L. Zhao, Y.K. Wang, M.M. Wang, J.F. Yang, T. Zhang, Y. Xiong, X.P. Wang, Q.F. Fang, C.S. Liu, Tailoring mechanical properties of a CoCrNi medium-entropy alloy by controlling nanotwin-HCP lamellae and annealing twins, Mater. Sci. Eng. A 744 (2019) 241-246.

[11] H. Beladi, I.B. Timokhina, Y. Estrin, J. Kim, B.C. De Cooman, S.K. Kim, Orientation dependence of twinning and strain hardening behaviour of a high manganese twinning induced plasticity steel with polycrystalline structure, Acta Mater. 59 (2011) 7787-7799.

[12] Q. Lai, H. Yang, Y. Wei, H. Zhou, L. Xiao, H. Ying, S. Lan, Z. You, Z. Kou, T. Feng, Q. Lu, P. Jacques, T. Pardoen, Transformation plasticity in high strength, ductile ultrafine-grained FeMn alloy processed by heavy ausforming, Int. J. Plasticity 148 (2022) 103151.

[13] J.W.Christian, S.Mahajan, Deformation twinning, Progress in Materials Science 39 (1995) 1-157.

[14] J.A. Venables, Deformation twinning in face-centred cubic metals, Philos. Mag. 6 (1961) 379-396.

[15] J.B. Cohen, J. Weertman, A dislocation model for twinning in f.c.c. metals, Acta Metall. 11(1963) 996-998.

[16] T. Mori, H. Fujita, Dislocation reactions during deformation twinning in Cu-11at.% Al single crystals, Acta Metall. 28 (1980) 771-776.

[17] S.Mahajan, G.Y.Chin, Formation of defromation twins in fcc crystals, Acta Mater. 21 (1973) 1353-1363.

[18] J.A. Venables, The martensite transformation in stainless steel, Philos. Mag. A 7 (1962) 35-44.

[19] H. Fujita, S. Ueda, Stacking faults and f.c.c. (γ) → h.c.p. (ϵ) transformation in 18/8-type stainless steel, Acta Metall. 20 (1972) 759-767.

[20] S.Mahajan, M.L.Green, D.Brasen, A model for the fcc-hcp transformation, its application and experimental evidence, Metall. trans. A 8 (1976) 283-283.

[21] H. Idrissi, K. Renard, L. Ryelandt, D. Schryvers, P.J. Jacques, On the mechanism of twin formation in Fe-Mn-C TWIP steels, Acta Mater. 58 (2010) 2464-2476.

[22] H. Idrissi, K. Renard, D. Schryvers, P.J. Jacques, TEM investigation of the formation mechanism of deformation twins in Fe-Mn-Si-Al TWIP steels, Philos. Mag. 93 (2013) 4378-4391.

[23] Y.T. Zhu, X.Z. Liao, X.L. Wu, Deformation twinning in nanocrystalline materials, Prog. Mater Sci. 57 (2012) 1-62.

[24] S. Huang, H. Huang, W. Li, D. Kim, S. Lu, X. Li, E. Holmstrom, S.K. Kwon, L. Vitos, Twinning in metastable high-entropy alloys, Nat. Commun. 9 (2018) 2381.

[25] J. Liu, C. Chen, Y. Xu, S. Wu, G. Wang, H. Wang, Y. Fang, L. Meng, Deformation twinning behaviors of the low stacking fault energy high-entropy alloy: An in-situ TEM study, Scr. Mater. 137 (2017) 9-12.

[26] R. Zhang, S. Zhao, J. Ding, Y. Chong, T. Jia, C. Ophus, M. Asta, R.O. Ritchie, A.M. Minor, Short-range order and its impact on the CrCoNi medium-entropy alloy, Nature 581 (2020) 283-287.

[27] C. Cayron, M. Den Hertog, L. Latu-Romain, C. Mouchet, C. Secouard, J.L. Rouviere, E. Rouviere, J.P. Simonato, Odd electron diffraction patterns in silicon nanowires and silicon thin films explained by microtwins and nanotwins, J Appl. Crystallogr. 42 (2009) 242-252.

[28] J.C. Li, W. Zheng, Q. Jiang, Stacking fault energy of iron-base shape memory alloys, Mater. Lett. 38 (1999) 275-277.

[29] J.M.Howe, U. Dahmen & R. Gronsky, Atomic mechanisms of precipitate plate growth, Philos. Mag. A 56 (1987) 31-61.

[30] A.M. Sanchez, J.A. Gott, H.A. Fonseka, Y. Zhang, H. Liu, R. Beanland, Stable Defects in Semiconductor Nanowires, Nano Lett. 18 (2018) 3081-3087.

[31] M. Sennour, S. Lartigue-Korinek, Y. Champion, M.J. Hÿtch, HRTEM study of defects in twin boundaries of ultra-fine grained copper, Philos. Mag. e 87 (2007) 1465-1486.

[32] H. Idrissi, K. Renard, D. Schryvers, P.J. Jacques, On the relationship between the twin internal structure and the work-hardening rate of TWIP steels, Scri. Mater. 63 (2010) 961-964.

[33] J.C. Williams, R.G. Baggerly, N.E. Paton, Deformation behavior of HCP Ti-Al alloy single crystals, Metall. Mater. Trans. A 33 (2002) 837-850.

[34] C. Herrera, D. Ponge, D. Raabe, Design of a novel Mn-based 1GPa duplex stainless TRIP steel with 60% ductility by a reduction of austenite stability, Acta Mater. 59 (2011) 4653-4664.

[35] Z. Li, K.G. Pradeep, Y. Deng, D. Raabe, C.C. Tasan, Metastable high-entropy dual-phase alloys overcome the strength-ductility trade-off, Nature 534 (2016) 227-30.

[36] P. Yu, R. Feng, J. Du, S. Shinzato, J.-P. Chou, B. Chen, Y.-C. Lo, P.K. Liaw, S. Ogata, A. Hu, Phase transformation assisted twinning in a face-centered-cubic FeCrNiCoAl high entropy alloy, Acta Mater. 181 (2019) 491-500.

[37] S. Curtze, V.T. Kuokkala, Dependence of tensile deformation behavior of TWIP steels on stacking fault energy, temperature and strain rate, Acta Mater. 58 (2010) 5129-5141.

[38] T.-H. Lee, E. Shin, C.-S. Oh, H.-Y. Ha, S.-J. Kim, Correlation between stacking fault energy and deformation microstructure in high-interstitial-alloyed austenitic steels, Acta Mater. 58 (2010) 3173-3186.

[39] L. Rémy, A. Pineau, Twinning and strain-induced f.c.c. → h.c.p. transformation on the mechanical properties of Co-Ni-Cr-Mo alloys, Mater. Sci. Eng. 26 (1976) 123-132.

[40] G. Meric de Bellefon, J.C. van Duysen, Tailoring plasticity of austenitic stainless steels for nuclear applications: Review of mechanisms controlling plasticity of austenitic steels below 400 °C, J Nucl. Mater. 475 (2016) 168-191.

[41] P. Chowdhury, H. Sehitoglu, Deformation physics of shape memory alloys – Fundamentals at atomistic frontier, Prog. Mater Sci. 88 (2017) 49-88.

[42] T.M. Smith, M.S. Hooshmand, B.D. Esser, F. Otto, D.W. McComb, E.P. George, M. Ghazisaeidi, M.J. Mills, Atomic-scale characterization and modeling of 60° dislocations in a high-entropy alloy, Acta Mater. 110 (2016) 352-363.

[43] T.C. Tisone, The concentration and temperature dependence of the stacking fault energy in face-centered cubic Co-Fe alloys, Acta Metall. 21 (1973) 229-236

[44] H. Idrissi, L. Ryelandt, M. Veron, D. Schryvers, P.J. Jacques, Is there a relationship between the stacking fault character and the activated mode of plasticity of Fe-Mn-based austenitic steels?, Scr. Mater. 60 (2009) 941-944.

[45] J. Wang, H. Huang, Shockley partial dislocations to twin: Another formation mechanism and generic driving force, Appl. Phys. Lett. 85 (2004) 5983-5985.

[46] Y.J. Xu, K. Du, C.Y. Cui, H.Q. Ye, Deformation twinning with zero macroscopic strain in a coarse-grained Ni–Co-based superalloy, Scr. Mater. 77 (2014) 71-74.

[47] L. Wang, P. Guan, J. Teng, P. Liu, D. Chen, W. Xie, D. Kong, S. Zhang, T. Zhu, Z. Zhang, E. Ma, M. Chen, X. Han, New twinning route in face-centered cubic nanocrystalline metals, Nat. Commun. 8 (2017) 2142.